Self-assembly, dynamics, and structure of Si magic clusters

Weijie Ong,[1,2] Eng Soon Tok,[1,2,*] Harman Johll,[3] and Hway Chuan Kang[3]
[1]*Department of Physics, National University of Singapore, Singapore 119260, Singapore*
[2]*Institute of Materials Research and Engineering, 3 Research Link, Singapore 117602, Singapore*
[3]*Department of Chemistry, National University of Singapore, Singapore 119260, Singapore*
(Received 11 February 2009; revised manuscript received 26 May 2009; published 29 June 2009)

We demonstrate the preferential formation and self-assembly of monodisperse Si magic clusters (X_4) of size $\sim 13.5 \pm 0.5$ Å on Si(111)-(7×7) surface using scanning tunneling microscope. The growth process is observed to occur via a stepwise assembly of planarized Si tetramers (X_1) formed from Si adatoms deposited at room temperature, leading to Si tetraclusters (X_2) (size $\sim 4.6 \pm 0.5$ Å) and culminating in tetracluster dimer (X_3) and trimer (X_4) formations as the surface is being annealed progressively to 150 °C. The respective cluster species density distribution at each annealing temperature also shows the preferential formation of $X_1 \rightarrow X_2 \rightarrow X_3 \rightarrow X_4$ at higher temperatures, which we describe using surface reaction schemes; $X_1 \rightarrow X_2$, $X_2 + X_2 \rightarrow X_3$, and $X_2 + X_3 \rightarrow X_4$. We determine the activation and formation energies for respective cluster species and elucidate the formation energetics and dynamics of tetraclusters which function unequivocally as fundamental building blocks in the self-assembly of stable Si magic clusters. Finally, we resolve the structure of the Si magic cluster to comprise three tetraclusters or $n=12$ Si atoms taking into consideration (i) cluster symmetry and alignment, (ii) close packing, and (iii) minimization of dangling bonds.

DOI: 10.1103/PhysRevB.79.235439 PACS number(s): 68.47.Fg, 68.35.Ja, 68.37.−d, 81.16.Dn

I. INTRODUCTION

The composition of a "magic" number of atoms captured in a closed shell configuration known as magic clusters have been found to exhibit unique stability and physical and electronic properties distinct from the bulk.[1] Formation of substrate supported magic clusters thus presents a progressive platform for device miniaturization. This has in turn attracted keen interest from industries such as microelectronics, magnetic data storage, and atomically precise manufacturing.[2–4] Considerable numbers of work on magic clusters of various material systems have thus been reported in a bid to create well-ordered monodispersed nanostructures.[5–11] These range from homogeneous metallic systems [e.g., Ag/Ag (100) and Pt/Pt (110) (Refs. 8 and 9)] to semiconducting systems [e.g., Si/Si (111) and Si/SiC (Refs. 12–15)] as well as heterogeneous systems comprising of mixed metal/semiconducting materials [e.g., In/Si (001) and Ga, In, Ag, Mn, Pb, and Co-Si/Si (111) (Refs. 11 and 16–19)]. With current technology largely entrenched in Si as the incumbent technological raw material, it is no surprise that Si magic clusters on Si substrates have attracted significant interest.

The observation of Si magic clusters on Si (111) has been previously reported by Tsong *et al.*[12–14] While Tsong *et al.*[12–14] provided a detailed study analyzing the diffusion characteristics of Si magic clusters in terms of the cluster hopping mechanism and electromigration effects as well as the energetics involved in cluster mobility, they did not however address the origin of Si magic clusters and how these clusters are formed in the first place on the Si (111) surface. Most of the other works on Si magic clusters up to now have been focused essentially on cluster dynamics and have overlooked this aspect of work. The lack of progress in this area inevitably makes it difficult to achieve control over the shape, size, monodispersity, as well as spatial ordering of Si magic clusters required for atomically precise architecture or effective device applications. As the formation of these clusters in terms of how they can be preferentially grown or manufactured to achieve well-ordered cluster arrays have not been adequately addressed,[20–22] this particular phase of Si material remains unexploited in spite of its technological potential.

In fact the structure of these magic clusters in terms of its size, shape, and composition of Si atoms is also unresolved. In the work of Tsong *et al.*,[13] while unable to ascertain the magic number of Si atoms per cluster, they proposed an estimate ranging between 9 and 15 from the dynamic behavior of clusters at step edges. However they did not correlate the size and shape of individual clusters, and they were also unable to resolve the atomic structure of the Si magic clusters. Several Si magic cluster structures have been predicted theoretically,[23–35] with varying geometries such as ring, prism, and octahedron structures, for different numbers of Si_n ($4 \leq n \leq 20$) where n is number of Si atoms per cluster. These theoretical calculations have also showed that clusters with different numbers of Si atoms display different bonding structures and hence do not share similar electronic or physical properties.[23–35] However, these atomic models only account for freestanding clusters in idealized minimum energy structures and do not accurately represent magic clusters existing on reconstructed surfaces. It is anticipated that the bonding characteristics of these proposed Si clusters may be altered with the introduction of an underlying substrate surface potential.

In this work, we will demonstrate how monodisperse Si magic clusters of size $\sim 13.5 \pm 0.5$ Å exhibiting localized spatial ordering can be achieved directly from Si adatoms deposited on a Si(111)-(7×7) template using a typical molecular-beam epitaxy solid source. We will show that the formation of the Si magic cluster architecture consisting of $n=12$ Si adatoms, occurs via a stepwise assembly of Si tetraclusters which function as fundamental building blocks instead of Si adatoms. By determining and understanding the

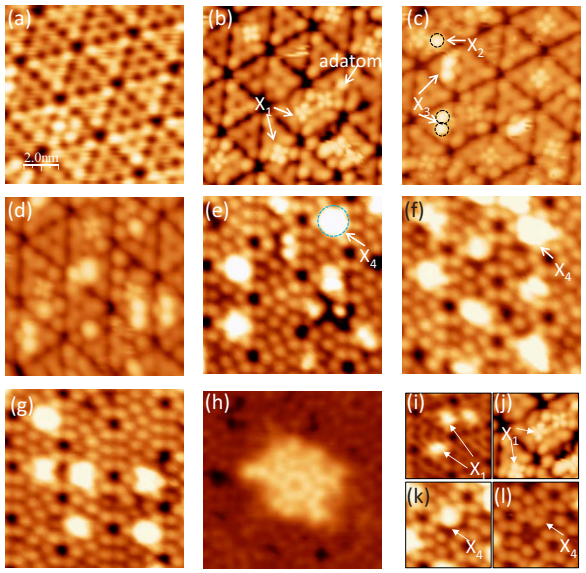

FIG. 1. (Color online) (a)–(i) show 10 nm×10 nm STM scans of (a) clean (7×7)-Si(111) surface, (b) 0.2 ML of Si deposited at room temperature, and the surface annealed for 30 min to (c) 70, (d) 100, (e) 130, (f) 150, (g) 200, and (h) 400 °C. STM tunneling bias ranged from ±0.1 to 3.0 V with tunneling currents of ~0.1 nA. Figure (i) shows 6×6 nm^2 images of X_1 scanned with bias (i) −2.0 and (ii) +2.0 V and X_4 scanned with bias (iii) −1.0 and (iv) +1.0 V.

mechanism and energetics leading to the formation of magic clusters, we address the issues of control over cluster fabrication much needed in applications such as Si cluster array photoluminescence, quantum computing, and tandem photovoltaic cells or other Si-based microelectronics devices.[36–41]

II. EXPERIMENTAL

The experiments were carried *in situ* out in an ultrahigh vacuum (UHV) system with an OMICRON variable temperature scanning tunneling microscope (VT-STM), with an ambient pressure of 1.0×10^{-8} Pa. The samples were cut from *P*-doped *n*-type Si (111) single-crystal wafers with dopant concentration of $\sim10^{18}$ cm^{-3} supplied by Virginia Semiconductors. The details of our sample preparation have been previously discussed.[10,11] These samples were first chemically etched *ex situ* in 1:10 parts of 49% hydrofluoric (HF) acid to deionized water before outgassing for 8 h at ~300 °C in the UHV chamber. The sample is subsequently flashed to 1200 °C to remove surface oxides and obtain clean Si(111)-(7×7) surface.

0.2 monolayer (ML) of Si was then deposited on the sample at room temperature (RT) via a solid source evaporator followed by progressive annealing of the surface to 70, 100, 130, 150, 200, and 400 °C. For each temperature, the surface is annealed for a corresponding time periods equal to 1, 10, 30, 60, and 120 min, respectively. STM measurements were then made immediately after each annealing step at room temperature. For each temperature and annealing time, the number density of each respective surface feature (X_1, X_2, X_3, and X_4 indicated in Fig. 1) observed was also counted.

All the STM images were taken using constant current mode, with tunneling currents of 0.10–1.00 nA and biases of $-2.0\leq V\leq+2.0$ V applied to the sample. The dimension and periodicity analysis were performed with the use of the WSXM software (Nanotec Electronica SL Sizes). The size of magic clusters was determined from the separation between opposite fringes of the bright cluster protrusions. These measurements were also taken when the same cluster is scanned under different tunneling biases (ranging from −2.0 to +2.0 V), and the changes in size associated with the different biases is reflected in the error bar. This is to reduce any electronic effects associated with changes with the electron-density distribution.

III. RESULTS AND DISCUSSION

A. Dynamics of Si magic cluster self-assembly

Figure 1(a) shows a 10×10 nm^2 STM scan of the initial clean surface comprising of well-ordered (7×7) reconstruction prepared by *in situ* flashing of the Si (111) sample to 1200 °C, prior to Si deposition. Figure 1(b) shows the same surface after 0.2 ML of Si was deposited at RT via a solid Si source electron-beam evaporator. When the surface was scanned under negative tunneling bias ($V=-2.0$ V and $I=0.2$ nA), the STM scan shows that the surface is preferentially decorated by features existing on top of the (7×7) reconstruction, in the shape of a "clover-leaf" which we indicate as X_1 as shown in Fig. 1(i). On closer observation, we find that these X_1 features consist of four Si adatoms configured as a planarized tetramer possessing fourfold symmetry. These X_1 features are observed to be exclusively sited between the boundaries dissecting the Si(111)-(7×7) unit cells and are also aligned along the ⟨110⟩ direction. However when the surface was scanned under positive bias ($V=+2.0$ V and $I=0.2$ nA), as shown in Fig. 1(j), the X_1 features appeared as bright round protrusions with an average size of ~4.6±0.5 Å when measured with the LINE PROFILE software.

Upon heating the surface to 70 °C for 30 min [Fig. 1(c)], the negative tunneling bias STM scans show that while the clover-leaf shaped X_1 features are still seen, in addition we also observe bright and round protrusions of size ~4.6±0.5 Å. We identify them with the single black dotted circle as shown in Fig. 1(c) and assign these features as X_2. These X_2 features can now be found within the (7×7) unit cells instead of just sitting at the unit-cell boundaries. However when the surface is scanned under positive bias, the X_2 features were not shown to exhibit planarized appearances akin to the X_1 features. Hence we identify them as single tetraclusters originating from the X_1 planarized tetramers. These tetracluster features are also observed to occur as paired entities, which we indicate with two adjacent black dotted circles as shown in Fig. 1(c). Line profile measurements show that each bright round protrusion has an average size of ~4.6±0.5 Å and the average separation between the two protrusions is ~5.7±0.5 Å. Hence we identify this paired cluster entity as X_3 and attribute it to the attachment of two X_2 species. We also note that these X_3 species tend to be located within (7×7) unit cells with its orientation aligned

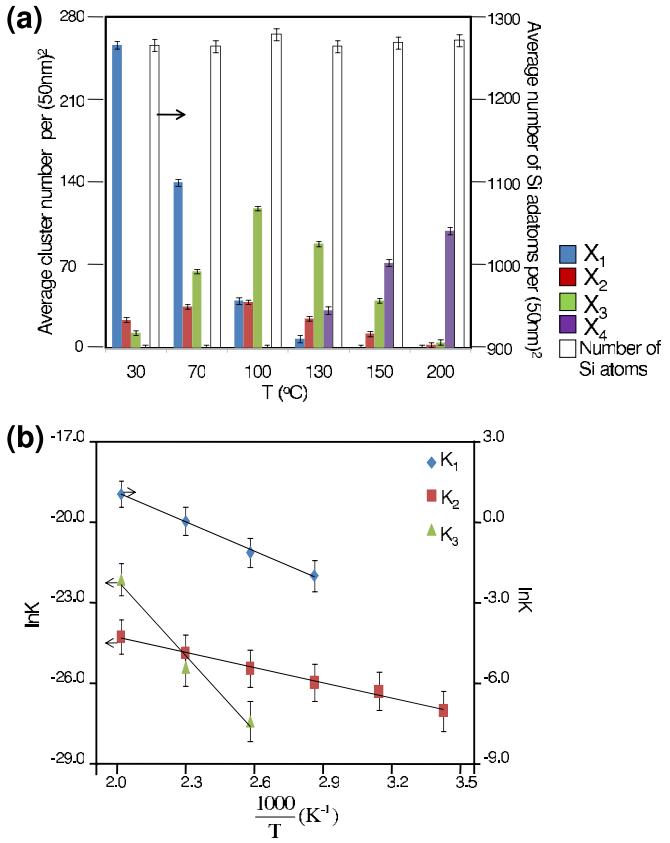

FIG. 2. (Color online) (a) shows the average number of each X_1, X_2, X_3, and X_4 species as well as total counted per (50 nm)^2 as a function of temperature. For each temperature, the surface is annealed until there are no further changes in the number density of each feature. Figure (b) shows the plot of ln K_i vs 1/T. (Note: the distribution remains the unchanged when the surface is annealed for 1, 10, 30, 60, and 120 min.)

to the unit-cell boundary in the ⟨110⟩ azimuthal direction.

When this same surface is heated to 100 °C as shown in Fig. 1(d), we continue to observe the coexistence of X_1, X_2, as well as X_3 species on the (7×7) surface structure. While the STM scans do not show significant difference in the type of surface features observed on surfaces annealed at different temperatures thus far, the number density of each configuration per (50 nm)^2 scan area as represented in Fig. 2(a) however shows that the density of X_1 has decreased, while X_2 and X_3 have both increased for $T=100$ °C when compared to that for $T=70$ °C. Hence we observe that a greater frequency of X_3 is observed, while X_1 continues to decrease as the surface is being annealed at higher temperatures.

In fact, when the surface is annealed to 130 °C the X_1 species ceases to be detected. In addition, we observe the occurrence of larger clusters, which we indicate with a blue dotted circle and correspondingly assign as X_4 as shown in Fig. 1(e). These X_4 species are found to be monodisperse and possess an average size of $\sim13.5\pm1.0$ Å, hence we identify them as Si magic clusters which exhibit similar shape and size to those observed by Tsong *et al.*[12–14] Although we still observe the occurrence of X_2 and X_3 species, the statistical counting of the cluster configurations show that this formation of X_4 coincides with a decrease in the number density of X_2 and X_3 as shown in Fig. 2(a).

Further heating of the same surface to 150 °C leads to the X_4 species dominating the surface structure as opposed to the earlier morphologies as shown by the STM scan in Fig. 1(f). We now also observe that X_4 species preferentially occupy the brighter faulted half unit cell (FUHC) of the (7×7) reconstruction. Consequently this spatial ordering leads to the occurrence of localized hexagonal Si magic cluster arrays as shown in Fig. 1(f). The negative tunneling bias STM scan of this surface as shown in Fig. 1(k) shows the magic clusters first appearing as a single bright maxima ($V=-1.0$ V and $I=0.2$ nA) before being resolved into a trimerlike arrangement of three smaller protrusions in positive tunneling bias scans ($V=+1.0$ V and $I=0.2$ nA) in Fig. 1(l). Line profile analysis of the cluster structure scanned under positive tunneling bias reveals that each smaller protrusion has an average size of $\sim4.6\pm0.5$ Å as well as a round shape which is similar to an X_2 tetracluster. This suggests that each magic cluster comprises of three tetraclusters locally arranged in a close-packed trimer configuration and thus consists of $n=12$ Si atoms in total.

When the surface is annealed to 200 °C, the surface is still preferentially dominated by X_4 species as shown by the STM scan in Fig. 1(g). Data from Fig. 2(a) show that the increase in the formation of X_4 is coupled with a decrease in number density of X_2 and X_3. The formation of a single magic cluster could therefore arise from the combination of a X_2 single tetracluster and a X_3 paired tetracluster. At this temperature, the cluster array as shown in Fig. 1(g) has become disordered and we no longer observe spatial ordering of Si magic clusters. In fact, the occurrence of Si magic clusters are not seen at 400 °C, and we observe the nucleation of two-dimensional islands with (7×7) reconstruction with average sizes of 30–50 Å as shown in the STM scan in Fig. 1(h). When we anneal the surface to 500 °C, the STM scans only show wide terraces of (7×7) reconstruction similar to the surface structure first observed in Fig. 1(a) with no other surface features observed. This suggests that this temperature is sufficient for Si diffusion to the steps resulting in the absence of Si surface features previously observed. Preferential growth of monodisperse Si magic clusters of size $\sim13.5\pm0.5$ Å can thus be precisely engineered by first depositing Si adatoms at RT followed by progressive annealing of the surface to 200 °C and not higher.

As observed, the growth process leading to the eventual formation of Si magic clusters involves the participation of X_1, X_2, and X_3 species. The histogram in Fig. 2(a) suggests that the dominant Si surface feature at 30 and 70 °C are planarized tetramers (X_1) and single tetraclusters (X_2), followed by paired tetraclusters (X_3) at 100 and 130 °C, and eventually magic clusters (X_4) at 150 and 200 °C. It should be noted that the number density for each respective cluster species (X_1, X_2, X_3, and X_4) at different temperatures shown in Fig. 2(a) is an average of data obtained from a series of measurements done by counting the number of each respective cluster species from five STM scans (50×50 nm^2) at corresponding annealing time periods of 1, 10, 30, 60, and 120 min. The upper limit and lower limit of number of species counted over the five scans was consistently $\leq\pm5\%$

TABLE I. Three surface reactions as well as corresponding energy barrier difference ΔE_i, relative formation energies $E(X_i)$, where $\Delta E_1=E_2-E_1$, $\Delta E_2=E_3-E_2$, $\Delta E_3=E_4-E_3$, and $E(X_1)$ is the formation energy of X_1 species from Si adatoms and respective pre-exponential ratios $\frac{A_i}{A_j}$. $E(X_i)^*$ is energy per cluster of four atoms.

Reaction	$X_1 \leftrightarrow X_2$	$X_2+X_2 \leftrightarrow X_3$	$X_2+X_3 \leftrightarrow X_4$
ΔE_i	$\Delta E_1=-0.09\pm0.01$ eV	$\Delta E_2=-0.05\pm0.01$ eV	$\Delta E_3=-0.22\pm0.01$ eV
$E(X_i)$	$E(X_2)=E(X_1)-0.09$ eV	$E(X_3)=2E(X_2)-0.05$ eV	$E(X_4)=E(X_2)+E(X_3)-0.22$ eV
$E(X_i)^*$	$E(X_2)^*=E(X_1)^*-0.09$ eV	$E(X_3)^*=E(X_1)^*-0.11$ eV	$E(X_4)^*=E(X_1)^*-0.12$ eV
$\frac{A_i}{A_j}$	$\frac{A_1}{A_2}=10.04$	$\frac{A_3}{A_4}=2.45\times 11^{-11}$ cm^2	$\frac{A_5}{A_6}=2.75\times10^{-9}$ cm^2

and constituted the error range for each number density derived. This was done for each annealing temperature of 30, 70, 100, 130, 150, and 200 °C. At each temperature, we found that the number density for each species and distribution shows no significant differences when data obtained from respective annealing time periods were compared. The distribution only changes when temperature increases. In addition, we also observed that the total number of Si atoms counted from each species on the average (~1280 per 50 $\times$50 nm^2) remains the same throughout the entire progressive annealing process from RT to 200 °C.

In order to rationalize the density distribution of each species at various temperatures, we therefore propose that the Si magic cluster self-assembly occurs by the following surface reaction scheme given by Eqs. (1)–(3), beginning with formation of X_2 from X_1, followed by a stepwise addition of X_2 culminating to form X_3 and X_4, respectively,

$$X_1 \overset{K_1^{eq}}{\leftrightarrow} X_2, \tag{1}$$

$$X_2 + X_2 \overset{K_2^{eq}}{\leftrightarrow} X_3, \tag{2}$$

$$X_2 + X_3 \overset{K_3^{eq}}{\leftrightarrow} X_4, \tag{3}$$

where

$$K_1^{eq} = \frac{[X_2]}{[X_1]} = \frac{A_1}{A_2}\exp\frac{(-E_1+E_2)}{kT}, \tag{4}$$

$$K_2^{eq} = \frac{[X_3]}{[X_2][X_2]} = \frac{A_3}{A_4}\exp\frac{(-E_2+E_3)}{kT}, \tag{5}$$

$$K_3^{eq} = \frac{[X_4]}{[X_2][X_3]} = \frac{A_5}{A_6}\exp\frac{(-E_3+E_4)}{kT}. \tag{6}$$

Our experimental data clearly shows that there is considerable diffusion occurring on the surface as Si atoms deposited at room temperature eventually becomes X_4. While we were not able to image diffusion species and processes in real time, the diffusion barrier attributed to Si adatoms moving across unit-cell boundaries on a Si(111)-(7$\times$7) was recently reported by Sato *et al.*[42] to be 1.14 eV (69–100 °C), using STM atom tracking methods. They described the Si adatom hop (R) as an attempt to diffuse from its initial position to the nearest-neighbor half unit and more significantly they were able to describe the diffusion length with the Arrhenius expression of $R=R_0\exp(-Ea/kT)$ using a prefactor of $R_0=10^{14.5\pm0.4}$ s^{-1} [where $E_a=1.14$ eV, $k=1.38\times10^{-23}$ J K^{-1}, and T=annealing temperature (K)]. While there have been other reports of Si diffusion barriers ranging from 1.96 to 2.64 eV,[12] however these were meant for Si magic cluster diffusion (X_4 species) and are therefore not an issue as the formation mechanism does not involve the diffusion of X_4. If we were to assume the diffusion barrier estimated by Sato *et al.*, we find that for 1 min of annealing for T=70, 100, and 130 °C, Si adatom may be expected to attempt 0.35, 7.74, and 108.24 hops/min, respectively. Si adatoms are thus highly mobile at the temperatures where $X_1 \rightarrow X_2$ (70 °C), $X_2+X_2 \rightarrow X_3$ (100 °C), and $X_2+X_3 \rightarrow X_4$ (130 °C) processes take place. Given that the surface when annealed to 1 min or to 2 h at each temperature shows no change in the number density for each species; the implication is that equilibrium is achieved at the respective temperatures and duration of annealing. The equilibrium constant K_i^{eq} (for i=1, 2, or 3) for each reaction [i.e., Eqs. (4)–(6)] can thus be determined from the surface density corresponding to each species $[X_i]$ (for i=1, 2, 3, or 4) captured in Fig. 2(a).

From the relationship $K_i^{eq} \approx \frac{A_i}{A_j}\exp\frac{(-E_i+E_j)}{kT}$, where E_i and E_j represent the respective energy barriers for the forward and backward reactions for the respective cluster species, we plot $\ln K_{eq}^i$ vs $\frac{1}{T}$ for the three reactions as shown in Fig. 2(b). A straight line can be drawn through each plot and therefore suggests that the proposed reactions scheme accurately describes the self-assembly mechanism of the Si magic cluster.

From the $\ln K_{eq}^i$ vs $\frac{1}{T}$ plots in Fig. 2(b), we obtain the activation energies of each reaction from the respective gradients (ΔE_i) of each plot, where $\Delta E_1=-0.09\pm0.01$ eV, $\Delta E_2=-0.05\pm0.01$ eV, and $\Delta E_3=-0.22\pm0.01$ eV as shown in Table I. The pre-exponential ratios (A_i/A_j) obtained appear reasonable when considering typical pre-exponential factors for unimolecular (~10^{12}–10^{13} s^{-1}) and bimolecular (~10^5–10^6 cm^2 s^{-1}) reactions.[43,44] Similarly, we also determine the relative formation energies $E(X_2)$, $E(X_3)$, and $E(X_4)$, associated with X_2 single tetraclusters, X_3 paired tetraclusters, and X_4 magic cluster species, respectively, from the surface reaction schemes given by Eqs. (1)–(3). The formation energies $E(X_2)=E(X_1)-0.09$ eV, $E(X_3)=2E(X_2)-0.05$ eV, and $E(X_4)=E(X_2)+E(X_3)-0.22$ eV as well as

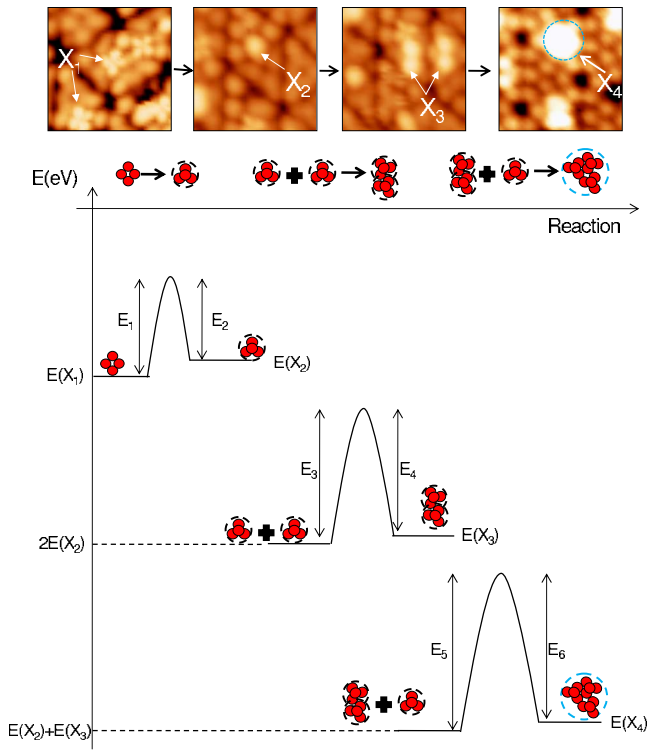

FIG. 3. (Color online) This shows 6×6 nm STM images as well as corresponding schematic model of the assembly of X_1, X_2, and X_3 tetracluster species to form X_4 Si magic cluster. Energy diagram shows relative stability of each species with respect to $E(X_1)$ associated with X_1 species.

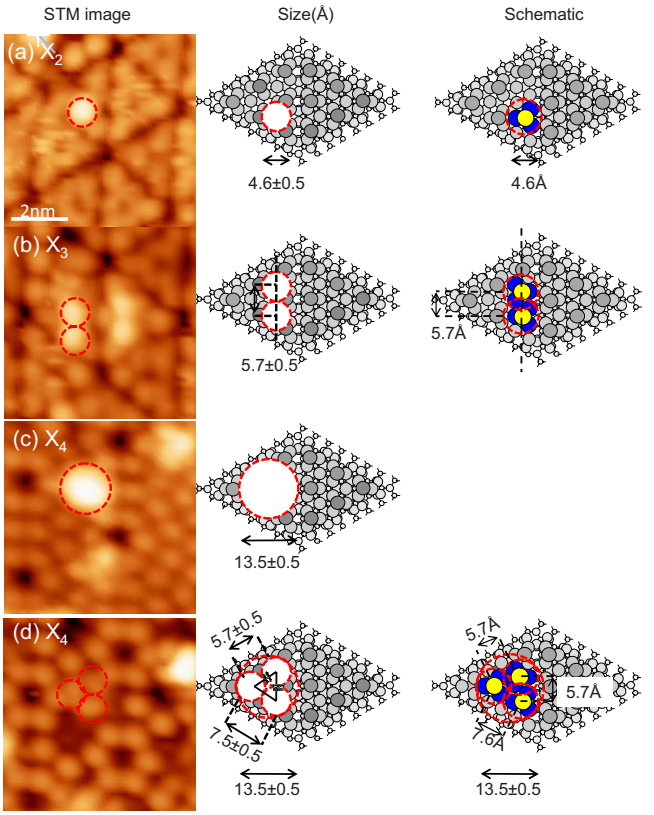

FIG. 4. (Color online) This shows the measured dimensions of tetracluster features indicated by dotted circles in (a) X_2 (size ~4.6±0.5 Å, height ~0.6±0.2 Å) (b) X_3 (size ~4.6±0.5 Å, height ~0.6±0.2 Å), (c) X_4 scanned in negative tunneling bias (V=−2.0 V) (size ~13.5±0.5 Å, height ~0.6±0.2 Å), and (d) X_4 scanned in positive tunneling bias (V=+2.0 V) (size ~4.6±0.5 Å, height ~0.6±0.2 Å). These features are represented as dotted circles and superimposed onto (7×7) unit-cell structures adjacent to the STM images. The proposed schematic models to describe the X_2, X_3, and X_4 species occupying top site positions on the (7×7) unit cell are shown in the third column.

corresponding expressions in terms of $E(X_1)^*$ are also shown in Table I [where $E(X_i)^*$ is energy per cluster of four atoms].

It appears that X_1 species, although slightly, is more stable than the other cluster species. The preferential formation of X_2, X_3, and X_4, respectively, at increasing temperatures [Fig. 2(a)] therefore suggest that the activation energy barriers associated with the formation of these tetracluster species (i.e., reactions 1, 2, and 3) are progressively larger. Together with the measured dimensions and alignments of X_2, X_3, and X_4 species, the reaction pathway leading to the self-assembly of magic clusters beginning with Si as tetraclusters is elucidated as shown in Fig. 3. In this figure, a schematic ball and stick diagrams illustrating the various surface reaction schemes show that X_2 is comprised of n=4 Si atoms and is formed from X_1, X_3 is comprised of n=8 Si atoms is formed from X_2+X_2, and X_4 is comprised of n=12 Si atoms and is formed from X_2+X_3. Herein, we show that the formation of monodisperse Si magic clusters occur from the stepwise addition of tetraclusters as fundamental building blocks in the reaction pathway-energy diagram as shown in Fig. 3.

B. Structural elucidation of Si magic clusters

Having established the dynamics, we now proceed to resolve the structure of the magic cluster by considering (i) the symmetry and alignment cluster with respect to (7×7) template, (ii) close packing, and (iii) minimization of dangling bond exhibited by X_2, X_3, and X_4 species. In order to describe the size of various surface features such as Si adatoms, tetraclusters, and magic clusters, we use STM line profile to measure the sizes of the corresponding features across three directions. This measurement is repeated for the same feature scanned under different biases (V=−2.0–+2.0 V) in order to obtain the average dimensions as well as error bars used to describe the size of surface features.

In Fig. 4, we summarize the measured average dimensions of the tetracluster features as indicated by the red dotted circles. Figure 4(a) shows the size of X_2 to be ~4.6±0.5 Å. Figure 4(b) shows the size of each individual cluster within X_3 to be ~4.6±0.5 Å. The X_3 tetracluster pair is also shown to be aligned in the ⟨110⟩ direction along the (7×7) unit-cell boundaries with a separation of ~5.7±0.5 Å. Figure 4(c) shows the size of X_4 scanned in negative tunneling bias to be ~13.5±0.5 Å. Figure 4(d) shows the size of each of the three clusters to be ~4.6±0.5 Å when scanned in positive tunneling bias. The three tetraclusters resolved within the X_4 species in Fig. 4(d) is also observed to be arranged in an isosceles configuration with separations of 5.7±0.5, 5.7±0.5, and 7.5±0.5 Å.

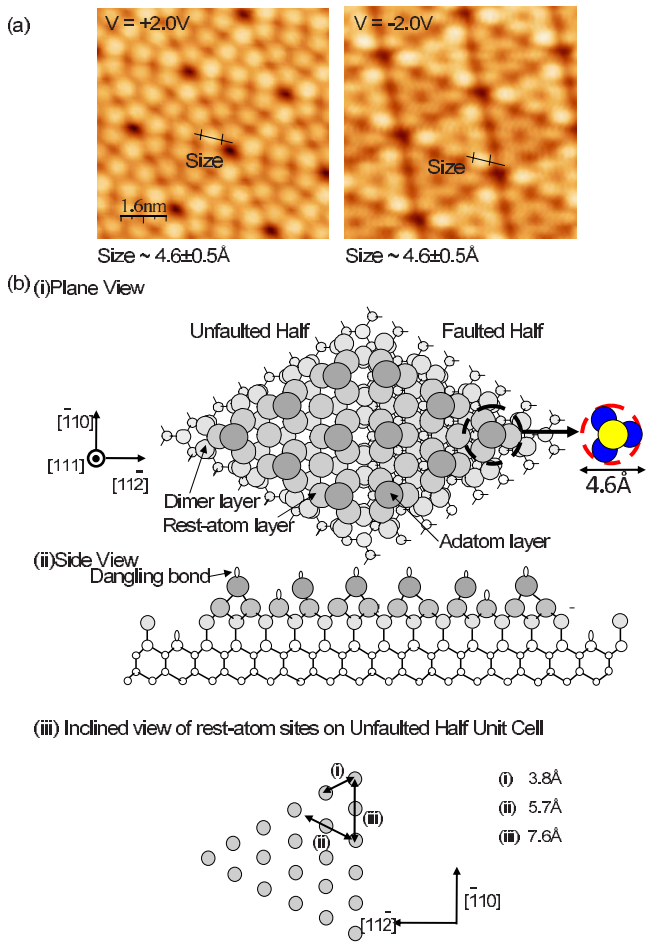

FIG. 5. (Color online) (a) shows the 10×10 nm^2 STM image of a (7×7) surface scanned at $V=+2.0$ V and $V=-2.0$ V. Average size and height of Si adatom is measured to be $\sim4.6\pm0.5$ and $\sim1.2\pm0.2$ Å (from the dimer layer) for both scans. (b) shows schematic diagram of the (7×7) unit cell in (i) plane and (ii) side views and (iii) inclined views indicating rest-atom sites.

In order to rationalize the size of an X_2 tetracluster, we correlate the size occupied by a single tetracluster with a similar spatial area on the (7×7) dimer-adatom-structure (DAS) structure. When we scan the clean (7×7) surface under different biases ranging from $-0.2\leq V\leq+2.0$ V, the average size of the electron cloud associated with the Si adatom of the (7×7) reconstruction is shown to be $\sim4.6\pm0.5$ Å. This is evident from the line profiles taken from the 10×10 nm^2 STM scans of the (7×7) surface scanned under tunneling bias $V=+2.0$ V and $V=-2.0$ V as shown in Fig. 5(a). As this electron cloud comprises of electronic state contributions from the three Si atoms bonded directly below in the rest-atom layer, hence the spatial area occupied by a Si adatom can be attributed to a Si atom sitting on top of three atoms in a tetrahedral configuration. When we analyze the (7×7) unit-cell DAS structure as shown in Fig. 5(b) (i) plane and (ii) side view, we find that the observed area occupied by a X_2 tetracluster (size $\sim4.6\pm0.5$ Å) when superimposed on the (7×7) unit cell as a dark dotted line coincides with the spatial area occupied by the Si adatom and the three underlying Si rest atoms. Hence

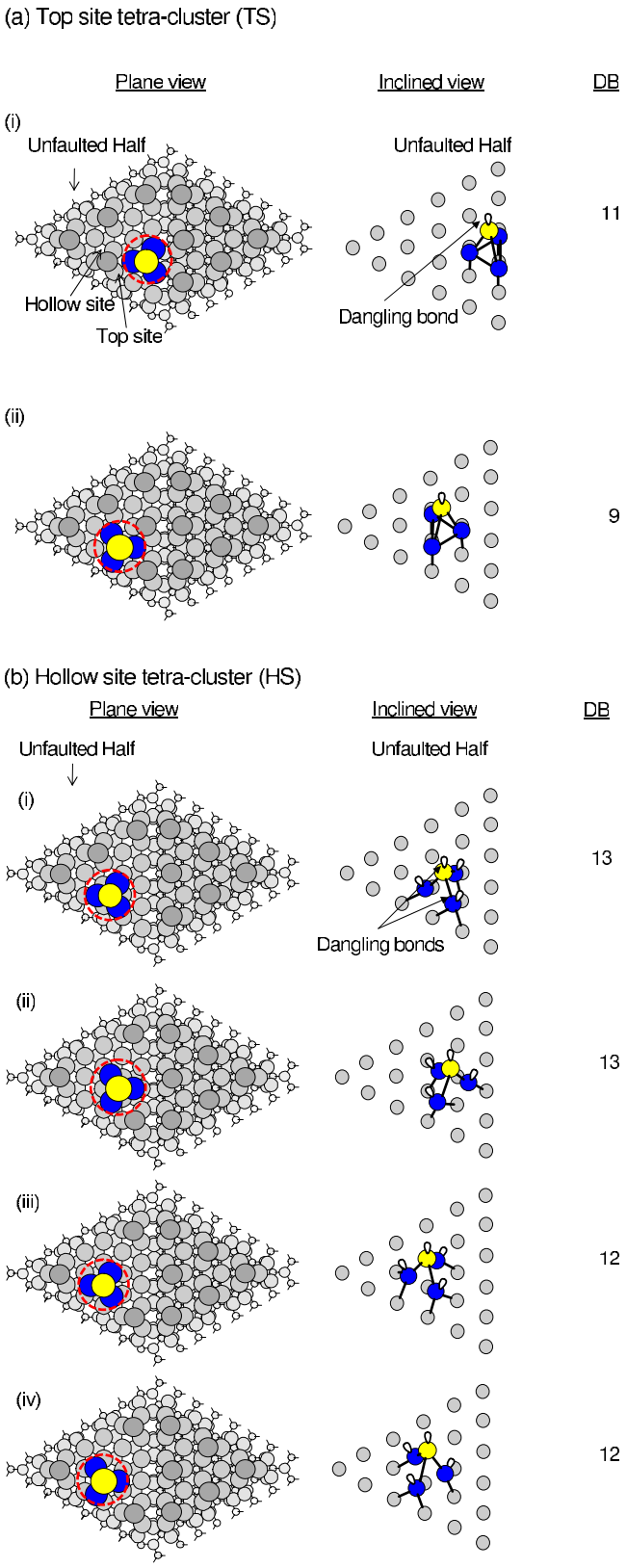

FIG. 6. (Color online) This shows the plane and inclined views of tetraclusters occupying (a) i–ii TSs and (b) i–iv HSs.

we illustrate the structure of a tetracluster by a yellow ball sitting on top of three blue ones occupying a spatial area of $\sim4.6\pm0.5$ Å in Fig. 5(b) (ii). In order to rationalize the

spatial alignment and dangling-bond minimization of the X_2, X_3, and X_4 cluster species on the (7×7) surface, we also illustrate in Fig. 5(b) (iii), a surface template comprising of only rest-atom sites from a (7×7) Faulted half unit cell (shown in inclined view).

We identify the two positions which a tetracluster may occupy on this template, as (i) top site (TS), where the tetracluster sits directly above a rest atom, or (ii) hollow sites (HSs), where the tetracluster occupies the position between rest-atom sites as shown in Figs. 6(a) and 6(b), respectively. Each TS tetracluster occupies three dangling bonds from the rest-atom layer resulting in one dangling bond per tetracluster, while each HS cluster occupies six dangling bonds from the rest-atom layer resulting in four dangling bonds per tetracluster. We show the different possible orientations of TS tetraclusters resulting in 11 and 9 dangling bonds per half (7×7) unit cell [Fig. 6(a) (i) and (ii)] as well as HS tetraclusters which result in 13, 13, 12, and 12 dangling bonds per half (7×7) unit cell [Fig. 6(b) (i)–(iv)]. Since TS tetraclusters tend to lead to a lower dangling-bond density on the (7×7) surface structure, hence we expect tetraclusters to prefer to occupy TS positions.

In the case of the X_3 species, after considering the alignment and separation ($\sim5.7\pm0.5$ Å) of paired tetracluster as well as dangling-bond minimization, we determine that the configuration of two adjacent TS clusters separated by ~5.7 Å aligned along $\langle110\rangle$ has the lowest dangling-bond density of 9 per half unit cell. Hence the structural model as shown in Fig. 7(a) best accounts for the X_3 species. We can thus rule out all other configurations which do not fulfill these considerations, such as the TS-HS tetracluster combination, for example, which is shown in Fig. 7(b), which has a separation of 7.6 Å and a higher dangling-bond density of 14 per half unit cell.

Figures 8(a)–8(c) show the three arrangements of tetracluster trimer configurations with lowest but equal dangling-bond densities of 13 per half unit cell. However when we again consider the observed alignment and dimensions for the X_4 species, we find that the structure in Fig. 8(a) consisting of three TS tetraclusters arranged in a close-packed isosceles formation with separations of 5.7, 5.7, and 7.5 Å is the best fit in describing the X_4 species. The other possible structural examples shown in Figs. 8(b) and 8(c) are not selected, as the tetracluster separations of 5.7, 7.5, and 7.5 Å are not observed.

In summary, the resolved structures of X_2, X_3, and X_4 species consisting of tetraclusters occupying top site positions are thus shown schematically as a ball and stick model in Fig. 4. In particular, the Si magic cluster structure with a size of $\sim13.5\pm0.5$ Å comprised of three TS tetraclusters arranged in a close-packed isosceles formation with separations of 5.7, 5.7, and 7.5 Å is determined to consist of $n=12$ Si atoms.

The ball and stick model proposed represents an attempt to elucidate the structure from consideration of dangling bonds and comparison of sizes of clusters observed from STM measurements. We understand that the experimental observations reported are confined within the constraints of the STM measurements as the existence of artifacts or distortion due to electronic effects could affect the accuracy of our size measurement. Nevertheless, we took caution during

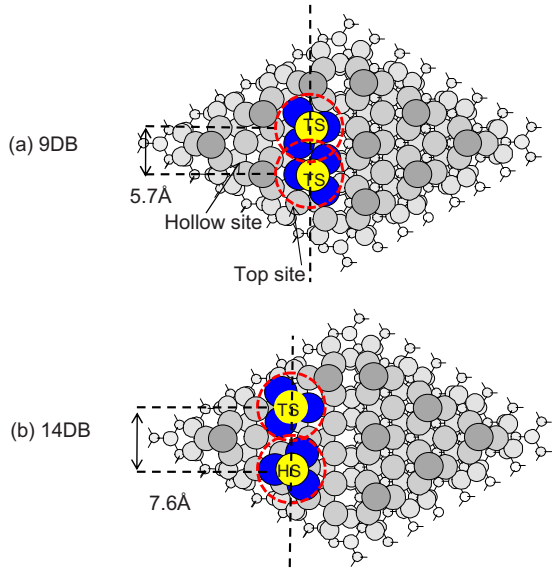

FIG. 7. (Color online) This shows top view schematic diagrams of X_3 species comprised of (a) two TS tetraclusters with no dangling bonds per half unit cell and (b) one TS and one HS tetraclusters with 14 dangling bonds per half unit cell.

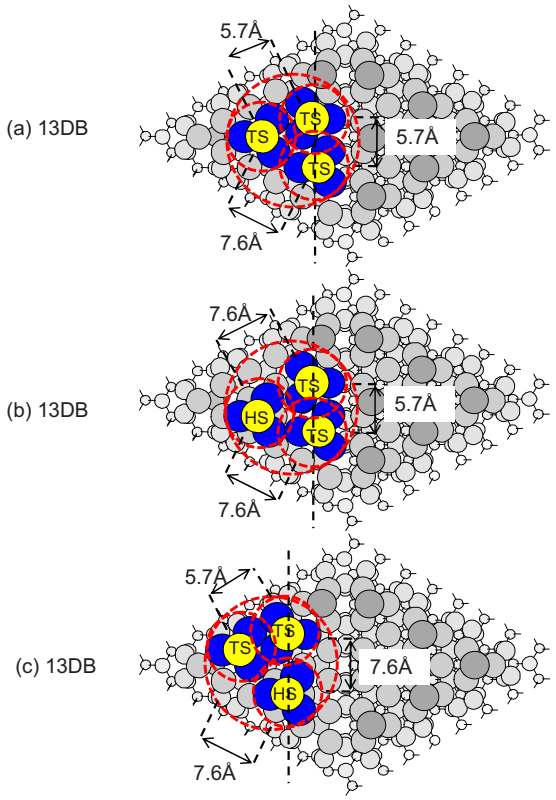

FIG. 8. (Color online) This shows top view schematic diagrams of X_4 species or magic clusters comprising of tetraclusters configured in (a) three TS tetraclusters with separations of 5.7, 5.7, and 7.5 Å, (b) two TS and one HS tetraclusters with separations of 5.7, 7.5, and 7.5 Å, and (c) two TS and one HS tetraclusters with separations of 5.7, 7.5, and 7.5 Å.

our scans by applying a slow scan speed through a large bias range to eliminate drift and electronic effects in ensuring that our images are topographical representations of the surface features. Clearly, a first-principles calculation of the magic cluster structure on a Si(111)-(7×7) surface template will be useful in confirming the cluster structure. Considering the large of number of atoms and different possible types of bonding configurations, a theoretical approach similar to that taken by Que *et al.*[45,46] may be necessary in order to solve this structure efficiently.

IV. CONCLUSION

In conclusion, we have addressed how to fabricate stable monodisperse magic clusters from Si adatoms deposited on (7×7)-Si(111) by the following:

(i) Demonstrating the self-assembly of Si magic cluster via the use of an atom source instead of a cluster source. In doing so, we avoid growth issues related to inconsistent cluster size and shape distributions typically attributed to the use of cluster source techniques.

(ii) Demonstrating the stability and self-assembly phenomena of Si magic clusters to form spatially well-ordered cluster arrays at low temperatures (<500 °C) thereby establishing Si magic clusters as a new phase within the framework of Si nanostructures which has potential for device applications.

(iii) Elucidating the growth mechanism of the Si magic cluster, which is shown to occur via a stepwise addition of tetraclusters as fundamental building blocks, where X_2 (comprised of $n=4$ Si atoms) is formed from X_1, X_3 (comprised of $n=8$ Si atoms) is formed from X_2+X_2, and X_4 (comprised of $n=12$ Si atoms) is formed from X_2+X_3. We also determine the respective relative formation energies from quantitative data to be $E(X_2)=E(X_1)-0.09$ eV, $E(X_3)=2E(X_2)-0.05$ eV, and $E(X_4)=E(X_2)+E(X_3)-0.22$ eV. It is unexpected that Si tetraclusters are fundamental building blocks in this growth process and not Si adatoms as anticipated.

(iv) Determining the structure of magic clusters in terms of its size ($\sim13.5\pm0.5$ Å), shape (three tetraclusters of size $\sim4.5\pm0.5$ Å occupying TS positions arranged in a close-packed isosceles formation with separations of 5.7, 5.7, and 7.5 Å) and number of Si atoms ($n=12$).

Thereby we have established Si magic clusters as a phase within the framework of Si nanostructures, where Si tetraclusters are fundamental building blocks in this growth process. The observation of tetraclusters grown from Si atoms deposited on Si (111) also suggests a natural tendency for Si adatoms to come together to form a Si_4 cluster. The agglomeration of the tetraclusters to form larger Si magic clusters also establishes the Si_4 structure as a critical and stable vehicle for Si mass transport and building block for the growth of Si magic clusters on Si (111). It is interesting to note the similar tetraclusters have also been observed separately on 6H-SiC (0001) surface[10] and also that Grass *et al.*[21] reported the existence of Si tetraclusters consisting of four Si atoms on HOPG. The Si_4 clusters were deposited from a cluster source and were shown to be stable against coalescence at room temperature similarly seen in this work. It will therefore be interesting to see if similar growth process leading to the assembly of Si magic clusters can also occur on an inert HOPG surface.

ACKNOWLEDGMENTS

This work was supported by NUS (Grant No. R-144-000-159-112) and IMRE.

*Corresponding author. phytokes@nus.edu.sg

[1] J. V. Barth, G. Constantini, and K. Kern, Nature (London) **437**, 671 (2005).
[2] M. T. Bohr, IEEE Trans. Nanotechnol. **1**, 56 (2002).
[3] D. A. Thomson and J. S. Best, IBM J. Res. Dev. **3**, 311 (2000).
[4] Zyvex Labs, Productive Nanosystems Technology Roadmap, 2007.
[5] H. Roder, E. Hahn, H. Brune, J. P. Bucher, and K. Kern, Nature (London) **366**, 141 (1993).
[6] J. A. Jensen, C. Yan, and A. C. Kummel, Science **267**, 493 (1995).
[7] J. M. Wen, S. L. Chang, J. W. Burnett, J. W. Evans, and P. A. Thel, Phys. Rev. Lett. **73**, 2591 (1994).
[8] T. R. Linderoth, S. Horch, L. Peterson, S. Helveg, E. Laegsgaard, I. Stensgaard, and F. Besenbacher, Phys. Rev. Lett. **82**, 1494 (1999).
[9] G. Rosenfeld, A. F. Becker, B. Poelsema, L. K. Verheij, and G. Cosma, Phys. Rev. Lett. **69**, 917 (1992).
[10] W. J. Ong, E. S. Tok, X. Hai, and A. T. S. Wee, Appl. Phys. Lett. **80**, 3406 (2002).
[11] W. J. Ong and E. S. Tok, Phys. Chem. Chem. Phys. **9**, 991 (2007).
[12] I. S. Hwang, M. S. Ho, and T. T. Tsong, Phys. Rev. Lett. **83**, 120 (1999).
[13] M. S. Ho, I. S. Hwang, and T. T. Tsong, Surf. Sci. **564**, 93 (2004).
[14] M. S. Ho, I. S. Hwang, and T. T. Tsong, J. Appl. Phys. **97**, 023522 (2005).
[15] E. S. Tok, W. J. Ong, and A. T. S. Wee, Surf. Sci. **558**, 145 (2004).
[16] M. Y. Lai and Y. L. Wang, Phys. Rev. Lett. **81**, 164 (1998).
[17] J. L. Li, J. F. Jia, X. J. Liang, X. Liu, J. Z. Wang, Q. K. Xue, Z. Q. Li, J. S. Tse, Z. Zhang, and S. B. Zhang, Phys. Rev. Lett. **88**, 066101 (2002).
[18] V. G. Kotlyar, A. V. Zotov, A. A. Saranin, E. N. Chukurov, T. V. Kasyanov, M. A. Cherevik, I. V. Pisarenko, H. Okado, M. Katayama, K. Oura, and V. G. Lifshits, Phys. Rev. Lett. **91**, 026104 (2003).
[19] S. C. Li, J. F. Jia, R. F. Dou, Q. K. Xue, I. G. Batyrev, and S. B. Zhang, Phys. Rev. Lett. **93**, 116103 (2004).
[20] Y. N. Yang and E. D. Willams, Phys. Rev. Lett. **72**, 1862 (1994).
[21] M. Grass, D. Fisher, M. Mathes, G. Gantefor, and P. Nielaba, Appl. Phys. Lett. **81**, 3810 (2002).
[22] H. Asaoka, V. Cherepanov, and B. Voigtlander, Surf. Sci. **588**,

19 (2005).
[23] C. M. Rohlfing and K. Raghavachari, Chem. Phys. Lett. **167**, 559 (1990).
[24] U. Rothlisberger, W. Andreoni, and P. Giannozi, J. Chem. Phys. **96**, 1248 (1992).
[25] M. F. Jarrold, Science **252**, 1085 (1991).
[26] R. P. Messmer and C. H. Patterson, Chem. Phys. Lett. **192**, 277 (1992).
[27] A. D. Mistriotis, G. E. Froudakis, P. Vendras, and N. Flytzanis, Phys. Rev. B **47**, 10648 (1993).
[28] E. Kaxiras and K. Jackson, Phys. Rev. Lett. **71**, 727 (1993).
[29] J. C. Grossman and L. Mitas, Phys. Rev. Lett. **74**, 1323 (1995).
[30] M. V. Ramakrishna and A. Bahel, J. Chem. Phys. **104**, 9833 (1996).
[31] I. Vasiliev, S. Ogut, and J. R. Chelikowsky, Phys. Rev. Lett. **78**, 4805 (1997).
[32] K.-M. Ho, A. A. Shvartsburg, B. Pan, Z.-Y. Lu, C.-Z. Wang, J. G. Wacker, J. L. Fye, and M. F. Jarrold, Nature (London) **392**, 582 (1998).
[33] Y. Luo, J. Zhao, and G. Wang, Phys. Rev. B **60**, 10703 (1999).
[34] B. Li and P. Cao, Phys. Rev. A **62**, 023201 (2000).
[35] I. Rata, A. A. Shvartsburg, M. Horoi, T. Frauenheim, K. W. M. Su, and K. A. Jackson, Phys. Rev. Lett. **85**, 546 (2000).
[36] M. A. Green, J. H. Zhao, A. H. Wang, P. J. Reece, and M. Gal, Nature (London) **412**, 805 (2001).
[37] A. T. Fiory and N. M. Ravindra, J. Electron. Mater. (to be published).
[38] S. Godefroo, M. Hayne, M. Jivanescu, A. Stesmans, M. Zacharias, O. I. Lebedev, G. Van Tendeloo, and V. V. Moshchalkov, Nat. Nanotechnol. **3**, 174 (2008).
[39] G. Conibeer, M. Green, E. C. Cho, D. Konig, Y. H. Cho, T. Fangsuwannarak, G. Scardera, E. Pink, Y. Huang, T. Puzzer, S. Huang, D. Song, C. Flynn, S. Park, X. Hao, and D. Mansfield, Thin Solid Films **516**, 6748 (2008).
[40] K. R. Catchpole, Philos. Trans. R. Soc. London **364**, 3493 (2006).
[41] A. Gajovic, D. Gracin, I. Djerdj, N. Tomasic, K. Juraic, and D. S. Su, Appl. Surf. Sci. **254**, 2748 (2008).
[42] T. Sato, S. Kitamura, and M. Iwatsuki, J. Vac. Sci. Technol. A **18**, 960 (2000).
[43] Z. Wang and E. G. Seebauer, Appl. Surf. Sci. **181**, 111 (2001).
[44] S. W. Benson, *Thermochemical Kinetics* (Wiley, New York, 1976).
[45] J. Z. Que, M. W. Radny, and P. V. Smith, Surf. Sci. **444**, 123 (2000).
[46] J. Z. Que, M. W. Radny, and P. V. Smith, Surf. Sci. **444**, 140 (2000).